RESEARCH ARTICLE
SPACE PHYSICS: IONOSPHERIC PHYSICS

Earth and Planetary Physics
9: 521–531, 2025
doi: 10.26464/epp2025038

Comprehensive evaluation of the vector magnetic field data from Macau Science Satellite-1A

XinYi Rang[1], Chao Xiong[1*], YuYang Huang[1], ChunYu Xu[1], FengJue Wang[1], BoHao Qian[1], Fan Yin[1], SiShan Song[1], Keke Zhang[2], and PengFei Liu[2]

[1]School of Earth and Space Science and Technology, Wuhan University, Wuhan 430072, China;

[2]Macau Institute of Space Technology and Application, Macau University of Science and Technology, Macao 999078, China

Key Points:

- The Macau Science Satellite-1A (MSS-1A) and Swarm A show high consistency in magnetic residuals to CHAOS-7 predictions (core and lithospheric field).
- The MSS-1A effectively captures magnetic signatures related to the magnetospheric ring current and ionospheric electrojet.
- The magnetic residuals of MSS-1A also show a diamagnetic effect caused by post-sunset equatorial plasma bubbles.

Citation: Rang, X. Y., Xiong, C., Huang, Y. Y., Xu, C. Y., Wang, F. J., Qian, B. H., Yin, F., Song, S. S., Zhang, K., and Liu, P. F. (2025). Comprehensive evaluation of the vector magnetic field data from Macau Science Satellite-1A. *Earth Planet. Phys.*, *9*(3), 521–531. http://doi.org/10.26464/epp2025038

Abstract: In this study, we present a comprehensive evaluation of the magnetic field measurements from the Vector Field Magnetometer (VFM) aboard the recently launched Macau Science Satellite-1 (MSS-1). One-year data from November 2, 2023, to November 1, 2024, are considered. The MSS-1 flies with a low inclination (41°) and is designed to provide high-resolution magnetic field measurements, especially for monitoring the evolution of the South Atlantic Anomaly. Earlier studies confirmed the possibility of using MSS-1A data to model the Earth's main magnetic field (e.g., Jiang Y et al., 2024). Therefore, in this study we focus on the magnetic signatures related to the external field, which are primarily associated with magnetospheric and ionospheric currents. The global distributions of the magnetic residuals from MSS-1A show a pattern consistent with that derived from the European Space Agency's Swarm A satellite. A statistical survey of the conjugated observations (with Δt < 5 min and ΔR < 150 km) between the two satellites showed that the difference between their magnetic residuals is within ±3 nanoteslas. By separating the magnetic residuals at the noon and midnight hours, we see that the MSS-1A data can effectively capture features of the magnetospheric and ionospheric currents, such as the magnetospheric ring current and ionospheric equatorial electrojet. Moreover, the magnetic residuals from MSS-1A show a diamagnetic effect caused by post-sunset equatorial plasma bubbles, which also suggests that the MSS-1A data have the potential to reveal the ionospheric structures. The comprehensive evaluations performed within this study demonstrate that the MSS-1A provides high-quality magnetic field data reaching the level of the Swarm satellite, which enables a deeper understanding of the modeling of Earth's magnetic field as well as monitoring of the magnetic environment.

Keywords: MSS satellite; magnetic field residuals; ring current; equatorial electrojet; diamagnetic effect

1. Introduction

The Earth's magnetic field is one of the most important geophysical fields, originating from its core, the lithosphere, and the surrounding space. It can be approximated by a dipole field, with its two magnetic poles located near the geographic poles, but they do not coincide exactly. As a critical protective barrier, the geomagnetic field shields the Earth from cosmic rays and high-energy particles in the solar wind, thereby safeguarding life on Earth from the harmful effects of these high-energy radiations (Tsareva et al., 2020). According to their origins, geomagnetic fields are generally categorized into internal and external fields. The internal field originates from magnetic materials and electric currents beneath the Earth's surface and can be further sorted into the core field, the lithospheric field, and induced fields. The external field originates from current systems, characterized by their global scale and spatiotemporal correlations. Currents can be broadly categorized based on their physical processes and distribution regions into interplanetary currents, magnetospheric currents, and ionospheric currents. Magnetospheric currents are further divided into magnetopause currents (e.g., Kivelson and Russell, 1995), magnetotail currents (e.g., Ness, 1965), ring currents (e.g., Dessler and Parker, 1959), and polar field-aligned currents (e.g., Iijima and Potemra, 1976a, b), with the latter serving as a critical coupling link between the magnetosphere and ionosphere. Field-aligned

First author: X. Y. Rang, 2022202120025@whu.edu.cn
Correspondence to: C. Xiong, xiongchao@whu.edu.cn
Received 31 JAN 2025; Accepted 19 MAR 2025.
First Published online 17 APR 2025.

currents are sometimes classified as ionospheric currents. Other ionospheric currents primarily include solar quiet (*Sq*) currents (e.g., Singer et al., 1951; Yabuzaki and Ogawa, 1974), the equatorial electrojet (EEJ; e.g., Chapman, 1951; Yamazaki and Maute, 2017), interhemispheric field-aligned currents (IHFAC; e.g., Fukushima, 1994; Olsen, 1997), and auroral electrojets (AEJ; e.g., Harang, 1946). Additionally, ionospheric currents encompass nightside horizontal zonal currents, gravity and pressure gradient currents (e.g., Alken et al., 2017), and diamagnetic currents induced by equatorial plasma bubbles (EPBs; e.g., Lühr et al., 1986a, b). These currents are generally weaker, causing magnetic field variations typically within ±10 nanoteslas (nT) or even <1 nT. From the perspective of magnetic field strength, the Earth's core magnetic field accounts for 95% of the total magnetic field, the lithospheric magnetic field accounts for about 4%, and the external and induced magnetic fields together make up only 1% of the total magnetic field (Xu WY, 2009). It is noteworthy that these external fields vary substantially over time, with their magnitude fluctuating from a few nT during geomagnetically quiet periods to several hundred or even thousands of nT during geomagnetic disturbances (Gonzalez et al., 1994). Wang YB et al. (2023) discussed influences of various space current systems on the geomagnetic field in near-Earth space through simulations, showing their significance in high-precision magnetic field modeling.

From the discussion above, it can be concluded that variations in the magnetic field are considered one of the key physical quantities for effective monitoring, diagnosis, and forecasting of the near-Earth space environment. Prior to the advent of satellites, magnetic field models were constructed using data from ground-based magnetometers, airborne surveys, and marine magnetic surveys. However, these methods were limited in spatial coverage and could not provide global magnetic field data over a short period (Yang YY et al., 2024). Since the 1950s, satellite observations have become the primary method for measuring the magnetic field in space. Compared with other measurement techniques, satellites are not limited by geographic location or surface weather conditions, enabling continuous measurements along their orbits and providing precise global magnetic field data (Xiong C et al., 2025). This capability has contributed substantially to the development of the magnetic field models (Alken et al., 2014). Low earth orbit satellite missions, from Magsat (Langel, 1979; Langel et al., 1980) to Swarm (Friis-Christensen et al., 2006), have greatly advanced Earth's magnetic field monitoring and enabled crucial studies of the recent evolution of the core magnetic field (Olsen and Stolle, 2012). With the development of China's space and satellite technologies, geomagnetic field detection satellites have also been launched. For instance, the China Seismo-Electromagnetic Satellite (CSES) was launched on February 2, 2018 (Shen XH et al., 2018), and the magnetic data it provides have been utilized for global geomagnetic field modeling (Yang YY et al., 2021).

The Macau Science Satellite-1 (MSS-1), launched on May 21, 2023, is a high-precision, low-inclination geomagnetic survey satellite. Unlike conventional magnetic survey satellites, which are limited by polar orbits, MSS-1A can provide high-resolution east–west magnetic field components. It also enables effective monitoring of the magnetic field in mid- and low-latitude regions, including the South Atlantic Anomaly (Yue YC et al., 2024). Recent research has demonstrated the advanced capabilities of MSS-1A. Jiang Y et al. (2024) derived the MSS-1 Initial Field Model (MIFM) by using 8 months of data from MSS-1A, supplemented by higher latitude field intensity measurements from the Swarm satellites. Further, Olsen (2025) describes the complementary nature of Swarm and MSS-1 satellites in geomagnetic field modelling and for monitoring large-scale magnetospheric contributions. Williams et al. (2025) performed an assessment of the lithospheric magnetic field by using the first year of MSS-1 data. Yao HB et al. (2025) combined magnetic field data from Swarm and MSS-1A, producing the self-consistent model of Earth's magnetic field and mantle conductivity. Additionally, Ren ZY et al. (2025) successfully extracted tidal-induced magnetic field signals from MSS-1A data, showing strong agreement with results from the Swarm and CryoSat satellites.

Although MSS-1A has demonstrated its capabilities in providing high-quality global magnetic field data, a comprehensive evaluation of its magnetic field data has not yet been performed. In this study, we evaluate the 1 Hz vector magnetic data from MSS-1A, focusing on the magnetic residual data processed by removing the core and lithospheric fields. Section 2 introduces the satellites and geomagnetic field models used for the MSS-1A evaluation, followed by presentation and discussion of the evaluation results in Sections 3 and 4. Finally, we summarize the main findings of this study in Section 5.

2. Datasets

The MSS-1 was launched on May 21, 2023, flying with a low-inclination (approximately 41°) and a near-circular orbit, at an initial altitude of approximately 450 km (Zhang K, 2023). The MSS-1 mission is designed to survey Earth's low-latitude magnetic field and monitor space environment changes. The MSS-1 is composed of two satellites (A and B). MSS-1A is equipped with a highly stable optical bench and three key instruments: a high-precision Fluxgate Magnetometer (FGM), a Vector Field Magnetometer (VFM), and a Coupled Dark State Magnetometer (CDSM). These instruments enable the satellite to measure the Earth's magnetic field with unprecedented accuracy. In this study, we evaluate the vector magnetic field data measured by the VFM, sampled at a rate of 1 Hz. As a comparison, we use Swarm A data, including magnetic field data from the VFM and electron density data from the Langmuir probes.

Figure 1 provides an overview of the altitude and local time (LT) evolution of the MSS-1A and Swarm A from November 2, 2023, to November 1, 2024. From Figure 1a, it can be observed that the orbit altitude of MSS-1A decreased by approximately 50 km over the year, whereas Swarm A experienced a reduction of approximately 20 km. This decrease is likely due to the elevated solar activity, which leads to higher atmospheric drag caused by perturbations and heating of the neutral thermosphere, thereby reducing the satellite's altitude (Nwankwo et al., 2015). Figure 1b shows LT coverage of MSS-1A and Swarm A. The MSS-1A requires approximately 26 days to cover 24 hours of LT, whereas Swarm A takes approximately 134 days, considering only their equatorial crossings. The low-inclination orbital characteristics of MSS-1A allow it

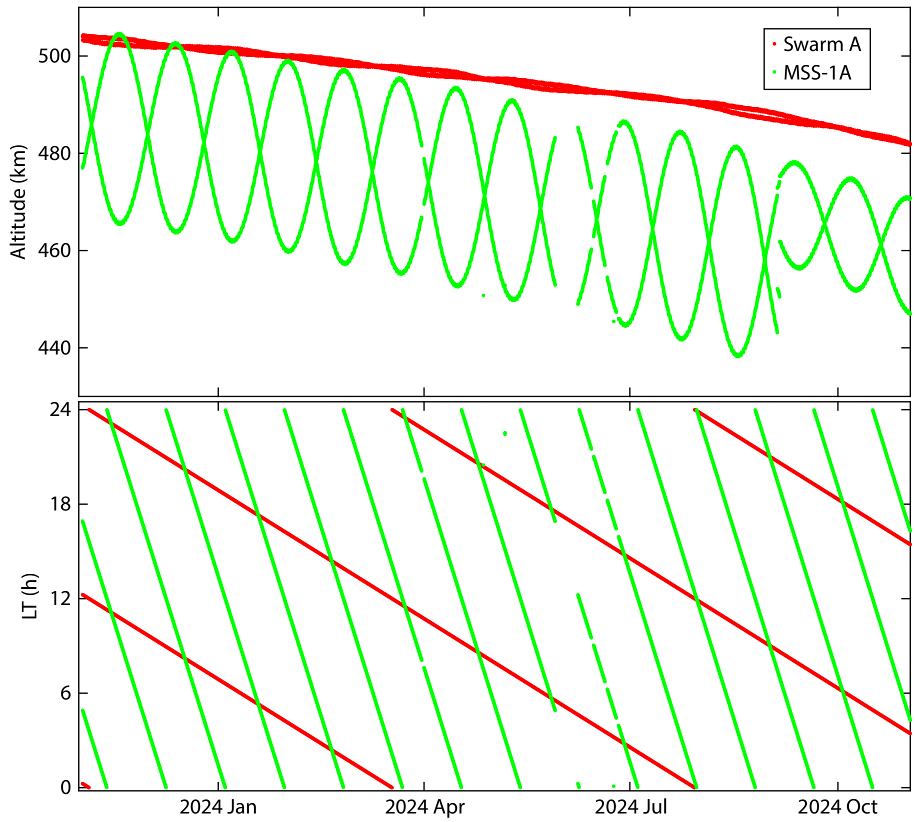

Figure 1. (a) Orbit altitude of MSS-1A's equatorial crossing. (b) Local time of MSS-1A's equatorial crossing. Both parameters are plotted from November 2, 2023, to November 1, 2024.

to sample the magnetic field at all local times in a relatively short period compared with that of Swarm, which has the advantage for studies requiring complete LT coverage, such as the magnetospheric ring current modeling and ionospheric signatures caused by tidal forcing from the lower atmosphere (Ou JM et al., 2024).

The CHAOS-7 model, developed by Danish Technological University (DTU), is a global geomagnetic field model designed to represent the Earth's main magnetic field and its secular variation. It combines ground-based observatory measurements and satellite observations from Swarm, CryoSat-2, CHAMP (Challenging Minisatellite Payload), SAC-C (Satélite de Aplicaciones Científicas-C), and Ørsted. The model consists of an internal field up to spherical harmonic degree 20, an LCS-1 lithospheric field model above degree 25, and an external field of degree 1 related to the Ring Current (RC) index (Olsen et al., 2014; Finlay et al., 2020). It is widely used in geophysical studies, space weather research, and magnetic anomaly mapping. In this study, we use the CHAOS-7 model to remove the contributions from the Earth's core and lithospheric fields to isolate the magnetic field generated by currents. The resulting residual magnetic field is primarily associated with magnetospheric and ionospheric currents.

3. Results

Considering the geographic latitude coverage of MSS-1A, Swarm A selected only the data within the latitude range of −41° to 41°N latitude in the following magnetic field data comparison. Figure 2 presents a time series of the geomagnetic activity condition and the residuals between the satellites' magnetic field data and CHAOS-7 predictions. Figures 2a and 2b show the *Kp* index and the geomagnetic index *Dst*. Figures 2c–2j display the ΔB_x, ΔB_y, and ΔB_z components in the North–East–Center (NEC) frame and the total of the residual magnetic field ΔB_f for MSS-1A and Swarm A, respectively. Both satellites exhibit substantial disturbances during geomagnetic storms, such as those on November 5, 2023, May 10, 2024, August 12, 2024, and October 10, 2024, with the residual total magnetic field reaching up to 200 nT. During geomagnetically quiet periods, the residual geomagnetic field components for both satellites remain within the range of tens of nT. This is primarily caused by the magnetic effects of magnetospheric currents and ionospheric currents.

As mentioned earlier, the magnetic residuals, processed by removing the core and lithospheric fields from CHAOS-7, reflect the structure of space currents. Figure 3 illustrates the geographic distribution of the magnetic residuals ΔB, represented by the median of all residuals within each grid bin with a bin size of 5° geographical latitude (GLAT) and 10° geographical longitude (GLON). Figures 3a and 3b display the global distribution of the three component residuals of MSS-1A and Swarm A, respectively, from November 2, 2023, to November 1, 2024. The *X*-component distributions of the two satellites exhibit an intense, narrow band that flows above the magnetic dip equator, directed southward, with a magnitude of approximately 40 nT. The *Y*-component primarily exhibits east–west variations, with negative values to the west of −70°E and positive values to the east. The *Z*-component in the northern hemisphere points toward the Earth's center, whereas the opposite is true in the southern hemisphere, with a

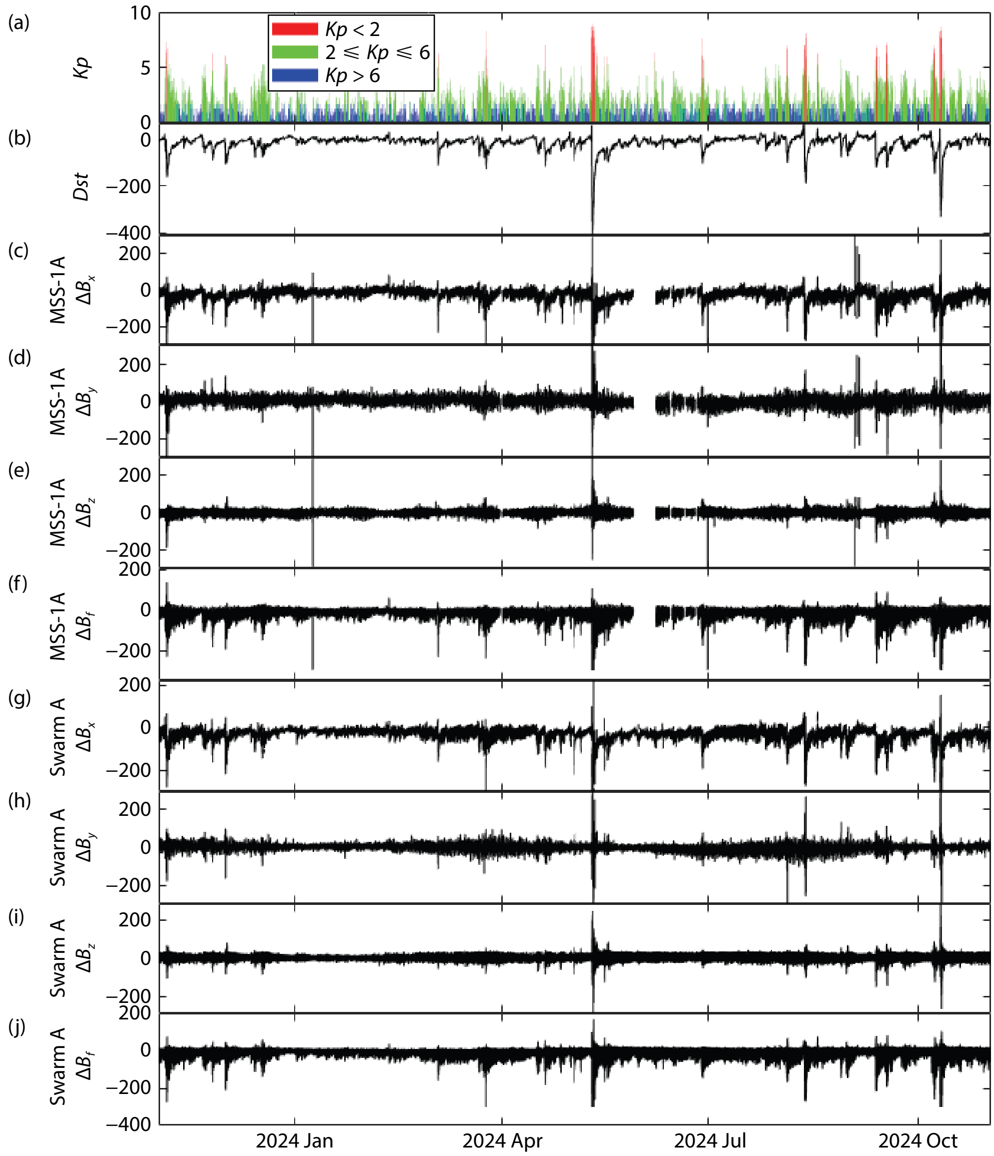

Figure 2. (a) *Kp* index. (b) *Dst* index. (c–f) Magnetic residuals to CHAOS-7 predictions (core and lithospheric field) in the three NEC components and the field magnitude for MSS-1A, and (g–j) the same for Swarm A. Each parameter is plotted from November 2, 2023, to November 1, 2024.

magnitude of approximately 10 nT in both hemispheres. Overall, the distribution maps of the three magnetic field components for MSS-1A and Swarm A are quite similar.

It is well-known that space currents are significantly influenced by geomagnetic activity and exhibit LT dependence. In this part, we focus on the distribution of magnetic residuals at noon (11:00–13:00 magnetic local time [MLT]) and midnight (23:00–01:00 MLT) during periods of low geomagnetic activity with $Kp \leq 2$. As shown in Figure 4, the median of the distribution is represented by the black line, with the dark gray shaded area indicating the interquartile range (25%–75%). The light gray area denotes the 1st–99th percentile range. Figure 4a illustrates that for all three components, the majority of the data (dark gray shaded area) show minimal deviation from the median, with differences of only around 15 nT. Each component exhibits distinct distribution characteristics. For example, the median of the *X*-component shows a distinct drop of approximately 20 nT at the magnetic equator, whereas the *Z*-component displays a noticeable reversal near the magnetic equator, changing from 11 nT to −14 nT within a latitude range of 7°. In contrast, at midnight the ΔB distribution does not exhibit any noticeable disturbances or variations, as shown in Figure 4b.

Figure 5 presents a comparison of magnetic field data between MSS-1A and Swarm A during their conjunction interval. We define a conjunction as when the spatial distance between MSS-1A and Swarm A was less than 150 km and the temporal interval in UTC (Coordinated Universal Time) was less than 5 minutes. Figures 5a and 5b provide examples of a conjunction event that occurred on October 3, 2023, from 11:41 to 11:47 UTC under geomagnetically quiet time. Figure 5a shows the geographical trajectory of this conjunction event, with both satellites in their descending orbits. The two satellites intersect at approximately −3°N latitude and −84°E longitude, with Swarm A crossing the location at around 11:42 UTC and MSS-1A crossing at approximately 11:47 UTC. The

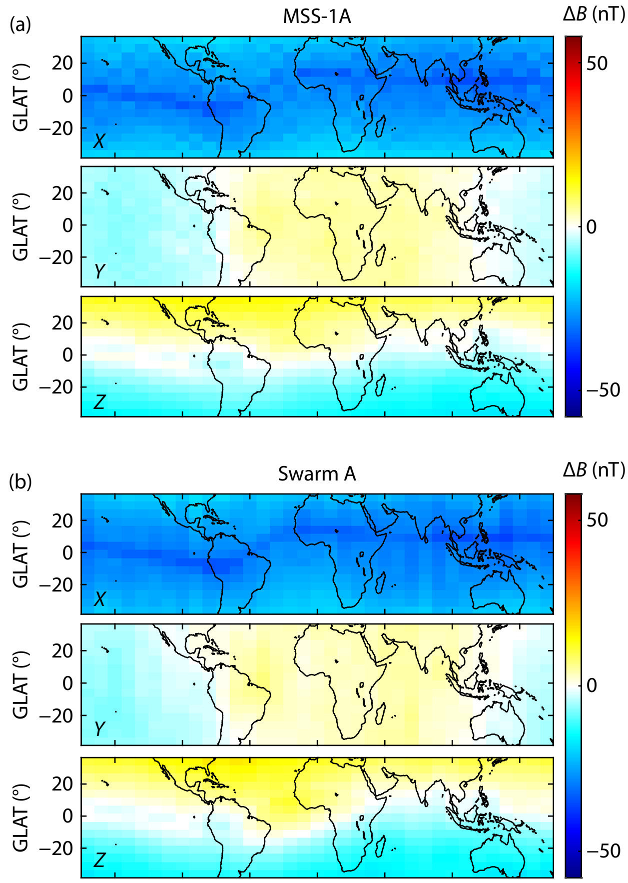

Figure 3. Geographic distribution of the magnetic residuals: (a) MSS-1A and (b) Swarm A.

close spatial and temporal alignment enables a direct comparison of their magnetic field data, providing an opportunity to verify and cross-check the quality of the magnetic field data of the two satellites. The red and green lines in Figure 5b represent the magnetic residuals, respectively, over time during this conjunction event. The average of the magnetic residuals between the two satellites is only about 2 nT. Additionally, we perform statistics on all conjunction events over the course of a year. Each conjunction event is represented by calculating the median of each satellite's magnetic residuals and then computing the difference between the two medians. From November 2, 2023, to November 1, 2024, a total of 1116 conjunction events occurred. To minimize the influence of geomagnetic storms and other disturbances on the statistical results, we select the processed data falling within the 10th to 90th percentile range. Figure 5c shows the distribution of the processed total magnetic field data within each bin of a grid with a bin size of 10° GLAT and 20° GLON. The majority of the data show variations within only ±1.5 nT. Such small differences between the MSS-1A and Swarm A observations further support the high quality of the magnetic data set of the MSS-1A mission.

4. Discussion

4.1 Magnetic Signatures Caused by Magnetospheric and Ionospheric Currents

Previous satellites have revealed that magnetospheric and ionospheric currents vary with LT (e.g., Lühr et al., 2003, 2017; Zhou YL and Lühr, 2017; Wang FJ et al., 2023). Therefore, in the time series shown in Figure 2, the magnetic residual components exhibit an envelope structure. To further illustrate the periodic structures within them, taking the Z-component as an example, we perform

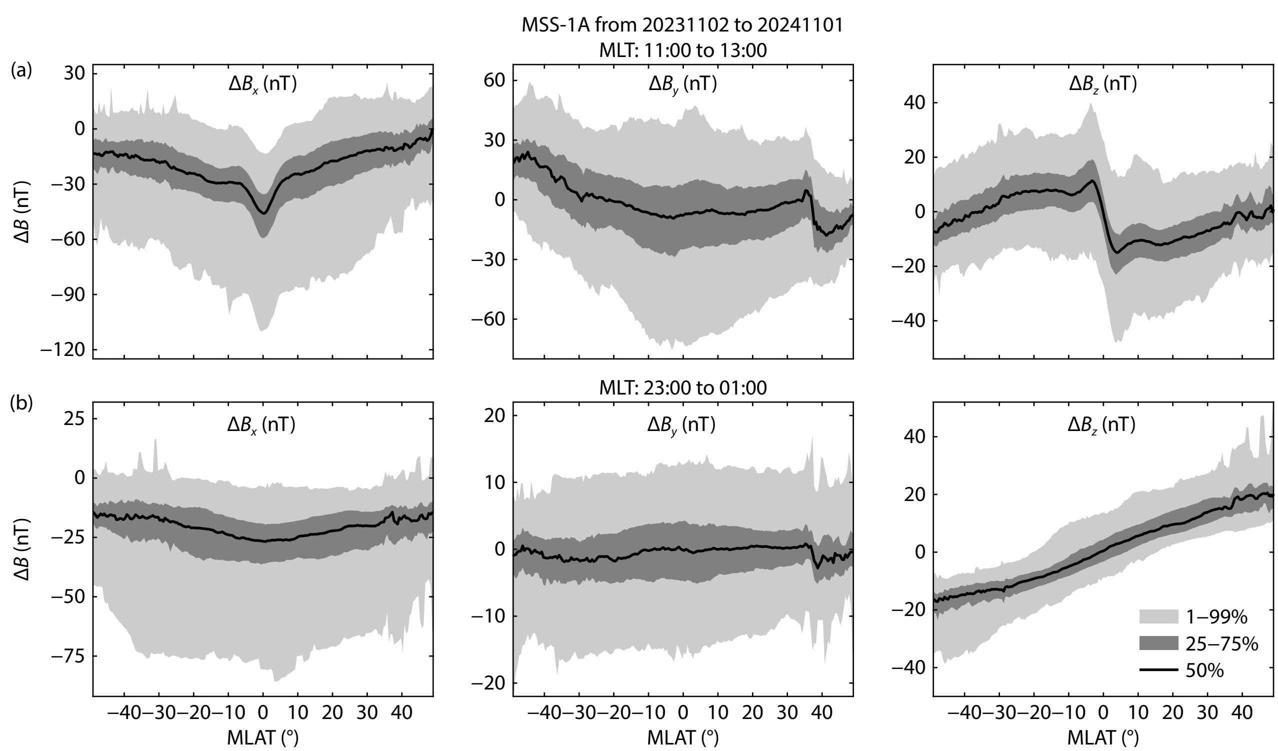

Figure 4. Magnetic residuals for (a) noon (11:00–13:00 MLT) and (b) midnight (23:00–01:00 MLT). The black line is the median, the dark gray shaded region is the interquartile range (25%–75%), and the light gray area denotes the 1st to 99th percentile range.

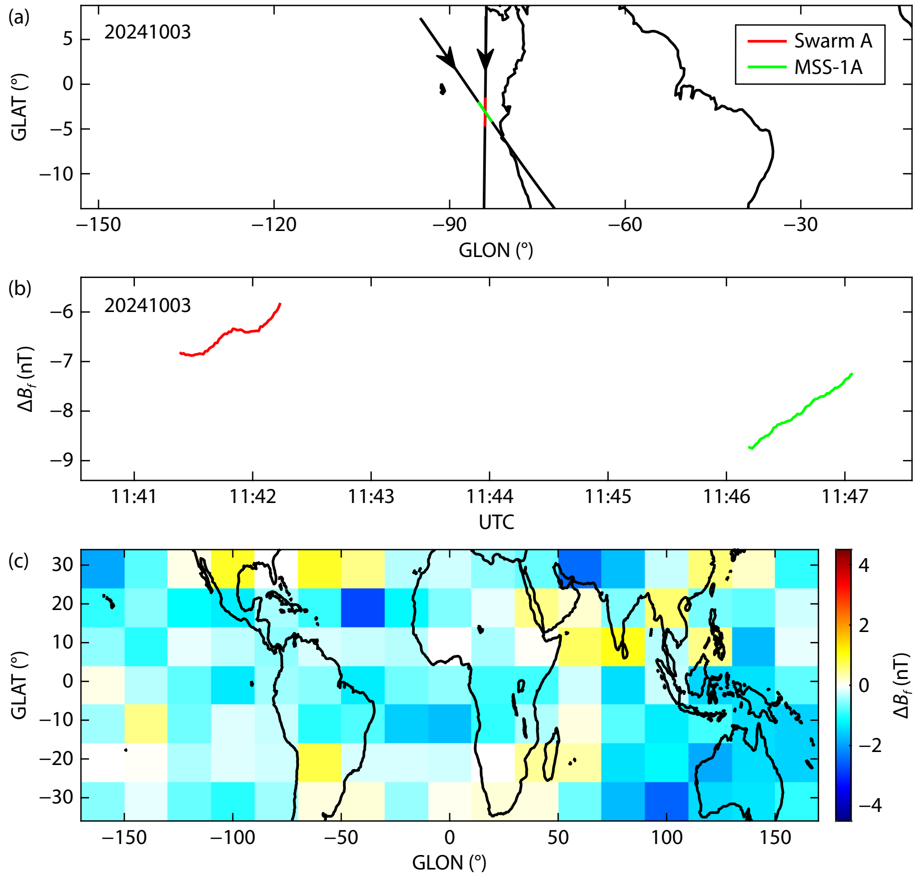

Figure 5. (a, b) Trajectory of a conjunction event between Swarm A and MSS-1A on October 3, 2024, with the total residual magnetic field. (c) Geographic distribution of the total residual magnetic field from all conjunction events between November 2, 2023, and November 1, 2024.

a spectral analysis on the magnetic residuals, as shown in Figure 6. The analysis revealed two frequency components related to the satellite orbit: one that varies with the satellite orbital period (approximately 1.56 hours) and the other that varies with the satellite orbital regression period (132.45 days for the Swarm A and 26.14 days for the MSS-1A). The satellite periods reflected in the spectrum are consistent with the features we derived from Figure 1, where the regression period of Swarm A is approximately 134 days and that of MSS-1A is 26 days, to cover all 24 hours of LT. The characteristics of magnetic field disturbances caused by currents with the satellite orbital regression period are also reflected in the geographic distribution maps, as shown in Figure 3. We can see clear vertical-banded stripes in the distribution of magnetic residuals of Swarm A, especially in the *X*-component. In contrast, MSS-1A, a low-inclination orbit satellite with a shorter regression period, shows a much smoother distribution of

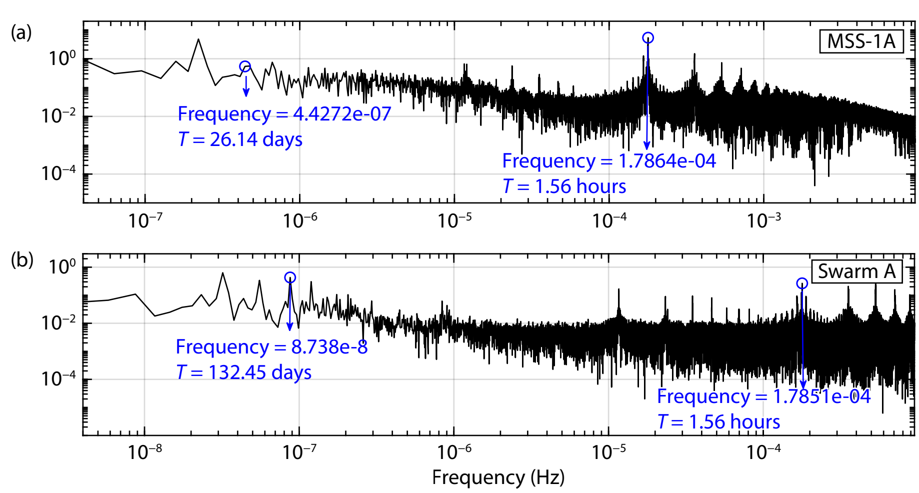

Figure 6. The spectral analysis of ΔB_z: (a) MSS-1A and (b) Swarm A. The blue text marks the satellite information for the orbital period and the orbital regression period.

magnetic residuals over one year.

Although the two satellites exhibit differences in the details of their magnetic residual distributions due to their distinct orbital characteristics, the overall macroscopic features are consistent. As shown in Figure 3, the *X*-component exhibits a pronounced minimum near the magnetic equator within a narrow latitude range of ±2°, closely resembling the distribution pattern of the EEJ, which is located at an altitude of approximately 105–110 km, well below the 450 km orbital altitude of MSS-1A. According to Ampere's law, the eastward EEJ generates a global southward magnetic disturbance, resulting in a downward perturbation in the northern hemisphere and an upward perturbation in the southern hemisphere. Similarly, the westward ring current, located at a higher altitude than MSS-1A, induces magnetic disturbances with the same directional characteristics as those observed by MSS-1A. These global distribution patterns of ΔB are not only affected by space currents but also associated with magnetic inclination and declination. For the *Z*-component, the magnetic inclination also contributes to the observed north–south hemisphere symmetry. The *Y*-component primarily exhibits longitudinal variations, with negative values to the west of −70°E and positive values to the east. This feature may be related to magnetic declination because the magnetic field lines are parallel to the meridian at −70°E, where B_y is zero.

Figure 4 shows the distribution characteristics of the magnetic residuals with magnetic latitude (MLAT). The statistical median suggests typical ionospheric features, whereas the shaded area reflects the day-to-day discrepancy. As shown in Figure 4a, at noon, significant variations in the *X*- and *Z*-components of the magnetic field are observed near the magnetic equator. The negative excursion in the *X*-component and the flip of the sign toward negative in the *Z*-component, directed toward the north, reflect the signatures of the EEJ. The amplitudes in both components, approximately 20 nT, are consistent with the signatures detected earlier in CHAMP and GRACE-FO (Gravity Recovery and Climate Experiment Follow-on; Lühr and Maus, 2006; Stolle et al., 2021). However, during nighttime, as solar ultraviolet radiation weakens and eventually disappears, the contribution of photoionization to the ionosphere gradually decreases, leading to a reduction in ionospheric conductivity (Prölss, 2004). Thus, no noticeable disturbances are observed in any of the three components, as shown in Figure 4b, which also indirectly confirms the reliability of the MSS-1A data.

4.2 Magnetic Signatures Related to Other Disturbances

Although the space currents are one important cause of magnetic signatures, other sources also cause magnetic disturbances, such as artificial signals from the satellite platform or EPBs. After a detailed analysis, we have repeated Figures 1 and 2 as Figure 7, but classify the magnetic signatures into different types. In general, the magnetic signatures from MSS-1A can be broadly classified into four types: (1) disturbances caused by magneto-

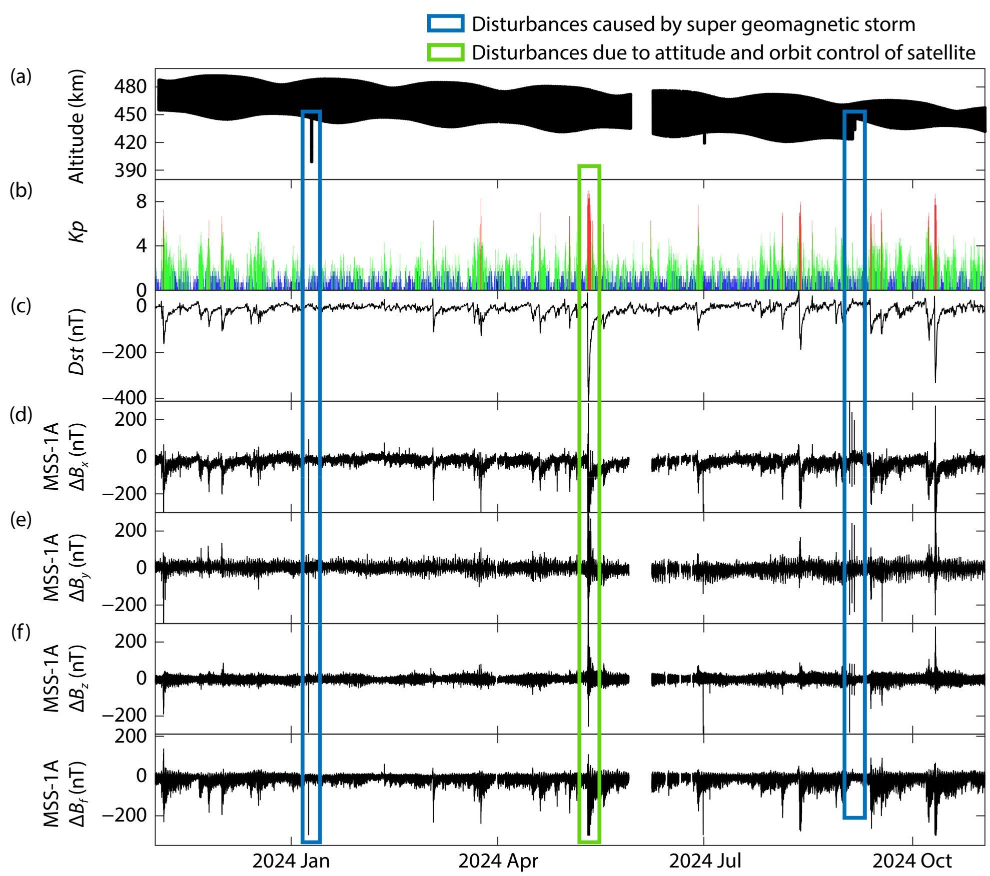

Figure 7. (a) Altitude of MSS-1A. (b) *Kp* index. (c) *Dst* index. (d–g) Magnetic residuals to CHAOS-7 predictions (core and lithospheric field) in the three NEC components and the field magnitude for MSS-1A. Each parameter is plotted from November 2, 2023, to November 1, 2024. The boxes represent different types of disturbances.

spheric and ionospheric currents; (2) disturbances caused by unmodeled patterns of CHAOS-7 (e.g., the magnetic signals from diamagnetic currents and ocean tides); (3) disturbances due to attitude and orbit control of the satellite; (4) disturbances of unknown origin.

We have already discussed the first type. Here, we would like to mention that although the MSS-1A and Swarm A flew at different MLT during the same geomagnetic storms, (e.g., on November 5, 2023, May 10, 2024, August 12,2024, and October 10, 2024), the enhancement of ring currents in the magnetosphere could induce disturbances of up to several hundred nT (green box shown in Figure 7). During geomagnetically quiet periods, the EEJ, driven by the eastward electric field on the dayside, also causes diurnal magnetic field variations of approximately 20 nT.

For the second type of disturbance, we take the perturbation induced by EPBs as an example. When charged particles enter the magnetic field, they generate magnetic moments that oppose the ambient field, resulting in a reduction of the background magnetic field, which is known as the diamagnetic effect. As demonstrated previously by Lühr et al. (2003) and Stolle et al. (2006) using high-precision magnetic field data and plasma density data observed by the CHAMP satellite, EPBs can cause a reduction of approximately 5 nT in the magnetic field at an altitude of 430 km. Figure 8 illustrates an EPB event observed simultaneously by MSS-1A and Swarm A. On November 15, 2023, the two satellites flew from south to north and intersected at 6°N, −55°E. Figure 8b shows the electron density data from Swarm A, with the red line highlighting the region of electron density depletion. For the magnetic field data, we follow the method outlined by Xu CY et al. (2024) by removing the CHAOS-7 model and filtering the magnetic residuals before transforming them into the mean field-aligned (MFA) coordinate system and showing the parallel component. As shown in Figure 8, from 02:47 to 02:50 UTC, Swarm A observed a magnetic disturbance of approximately 0.3 nT caused by the plasma bubble. Seventeen minutes later, MSS-1A passed through the same region of electron density depletion and observed the EPBs between 03:05 and 03:06 UTC,

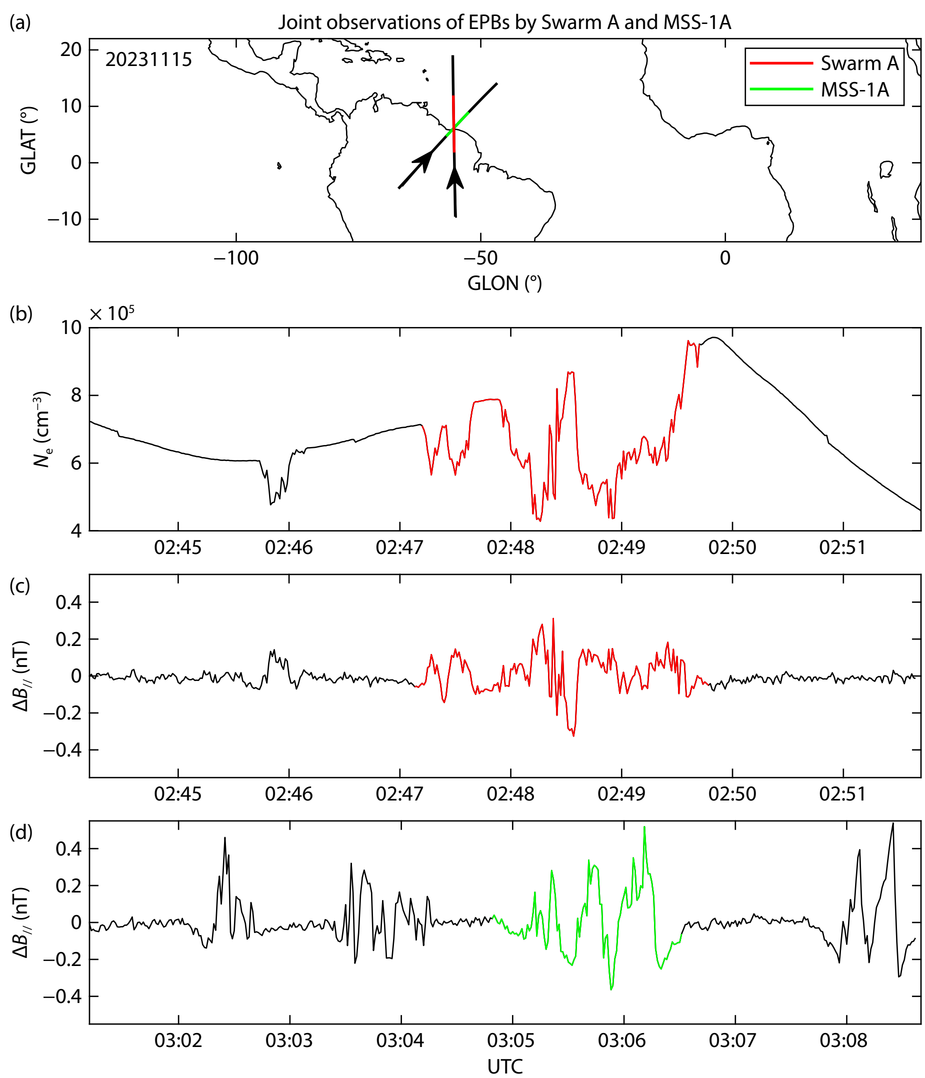

Figure 8. (a) Trajectory of EPBs observed during a single orbit with simultaneous observations by Swarm A and MSS-1A on November 15, 2023. (b) N_e from Swarm A. (c) $\Delta B_{//}$ profiles from Swarm A over UTC. (d) Similar to (c), but for MSS-1A. The colored lines in the figure highlight the parameters related to EPBs.

with a magnetic disturbance of approximately 0.4 nT. The EPBs would not be expected to undergo significant changes within such a short time frame. The longitudinal span of the EPBs was approximately 4°, and the east–west scale of the EPBs was approximately 440 km. Previous studies on EPBs have typically used polar-orbiting satellites (e.g., Xiong C et al., 2010; Xiong C and Lühr, 2023), which can analyze only the latitudinal scale of EPBs. As shown in Figure 8d, within just 6 minutes of MSS-1A's flight time, four depletion regions were observed. The low-inclination orbit of MSS-1A allows for rapid latitudinal coverage, with observations from MSS-1A providing a valuable new perspective for studying the morphology of EPBs and other ionospheric structures.

For the third type, we discuss the disturbances from the satellite itself. Although magnetometers undergo rigorous testing and calibration before launch, their accuracy can still be affected by variations in onboard electrical and electronic systems after deployment. Moreover, long-term in-orbit operation can lead to sensor degradation, particularly for vector magnetometers, as aging components and changing environmental conditions gradually render prelaunch calibration parameters obsolete, compromising data reliability. Therefore, in-orbit calibration is essential to ensure measurement accuracy and data reliability (Rother et al., 2005; Yin F, 2010; Yin F and Lühr, 2011). Some of these perturbations have clear and identifiable sources, such as issues with the mechanical link between the FGM and the star tracker (STR) leading to anomalies in the southernmost part of the nightside segment of CSES orbits (Yang YY et al., 2021). Here, we present two distinct cases caused by attitude and orbit control of the satellite. The first case occurred on January 8, 2024, when an anomalous altitude of 403 km was recorded. This anomaly resulted in a clear spike of magnetic disturbance exceeding 300 nT, as highlighted by the blue box on the left side of Figure 7. The second case took place on September 5, 2024, when a significant altitude adjustment of approximately 20 km was observed. This altitude change affected all three magnetic field components, each exhibiting variations exceeding 200 nT while the total magnetic field remained unchanged, as shown by the blue box on the right side of Figure 7.

Although for most of the magnetic signatures in MSS-1A, we already have good explanations, some signatures still need further investigation. These fall under the fourth kind of disturbances: disturbances of unknown origin. These signatures require a comprehensive physical and mathematical analysis of satellite operational states, environmental parameters, and orbital characteristics to be accurately identified (Yang YY et al., 2024). For example, all six subplots in Figure 4 show a noticeable drop in the magnetic field components at 37°N MLAT with a magnitude of 2 nT, along with high-frequency perturbations at 35°–50°N MLAT.

5. Summary

In this study, we provide a comprehensive evaluation of the 1 Hz vector magnetic data from the MSS-1A. Our analysis confirms that the MSS-1A can deliver high-quality magnetic survey data. The key findings from our comprehensive evaluation are as follows:

(1) The global distributions of all three components of magnetic residuals from MSS-1A show a pattern consistent with that derived from Swarm A, with the distribution of MSS-1A showing less LT dependence. A statistical comparison of conjugate observations between the two satellites indicates that the differences in their magnetic residuals are within ±3 nT.

(2) The MSS-1A is capable of capturing the characteristics of space currents, such as the magnetospheric ring current and ionospheric EEJ. By separating the magnetic residuals at the noon and midnight hours, we see features the EEJ causes in diurnal magnetic field variations of approximately 20 nT.

(3) The magnetic residuals of MSS-1A also show a diamagnetic effect caused by post-sunset EPBs. We provide an EPB event observed simultaneously by MSS-1A and Swarm A, highlighting the potential of MSS-1A to reveal the ionospheric structures.

(4) However, magnetic field data of MSS-1A also contain unidentified disturbances, such as a sudden drop at 37°N MLAT and high-frequency perturbations at 35°–50°N MLAT, which warrant further investigation.

Data Availability Statement

The MSS-1A magnetic field data can be downloaded from the Macau University of Science and Technology MSS website: https://mss.must.edu.mo. The Swarm magnetic field and electron density data can be downloaded from the European Space Agency Swarm website: https://earth.esa.int. The CHAOS-7 model can be downloaded from https://www.spacecenter.dk/files/magnetic-models/CHAOS-7. The *Dst* and *Kp* indexes can be accessed through the OMNIWeb Data Explorer: https://omniweb.gsfc.nasa.gov/form/omni_min.html.

Acknowledgments

This work was supported by the National Natural Science Foundation of China (Grant Nos. 42474200 and 42174186). Chao Xiong is supported by the Dragon 6 cooperation 2024–2028 (Project No. 95437).

References

Alken, P., Maus, S., Lühr, H., Redmon, R. J., Rich, F., Bowman, B., and O'Malley, S. M. (2014). Geomagnetic main field modeling with DMSP. *J. Geophys. Res.: Space Phys.*, *119*(5), 4010–4025. https://doi.org/10.1002/2013JA019754

Alken, P., Maute, A., and Richmond, A. D. (2017). The F-region gravity and pressure gradient current systems: A review. *Space Sci. Rev.*, *206*(1), 451–469. https://doi.org/10.1007/s11214-016-0266-z

Chapman, S. (1951). The equatorial electrojet as detected from the abnormal electric current distribution above Huancayo, Peru, and elsewhere. *Arch. Meteorol. Geophys. Bioklimatol. A*, *4*(1), 368–390. https://doi.org/10.1007/BF02246814

Dessler, A. J., and Parker, E. N. (1959). Hydromagnetic theory of geomagnetic storms. *J. Geophys. Res.*, *64*(12), 2239–2252. https://doi.org/10.1029/JZ064i012p02239

Finlay, C. C., Kloss, C., Olsen, N., Hammer, M. D., Tøffner-Clausen, L., Grayver, A., and Kuvshinov, A. (2020). The CHAOS-7 geomagnetic field model and observed changes in the South Atlantic Anomaly. *Earth Planets Space*, *72*(1), 156. https://doi.org/10.1186/s40623-020-01252-9

Friis-Christensen, E., Lühr, H., and Hulot, G. (2006). *Swarm*: A constellation to study the Earth's magnetic field. *Earth Planets Space*, *58*(4), 351–358. https://doi.org/10.1186/BF03351933

Fukushima, N. (1994). Some topics and historical episodes in geomagnetism and aeronomy. *J. Geophys.Res.: Space Phys.*, *99*(A10), 19113–19142. https://

doi.org/10.1029/94ja00102

Gonzalez, W. D., Joselyn, J. A., Kamide, Y., Kroehl, H. W., Rostoker, G., Tsurutani, B. T., and Vasyliunas, V. M. (1994). What is a geomagnetic storm?. *J. Geophys. Res.: Space Phys.*, *99*(A4), 5771–5792. https://doi.org/10.1029/93JA02867

Harang, L. (1946). The auroral luminosity-curve. *Terr. Magn. Atmos. Electr.*, *51*(3), 381–400. https://doi.org/10.1029/TE051i003p00381

Iijima, T., and Potemra, T. A. (1976a). The amplitude distribution of field-aligned currents at northern high latitudes observed by Triad. *J. Geophys.Res.: Space Phys.*, *81*(13), 2165–2174. https://doi.org/10.1029/ja081i013p02165

Iijima, T., and Potemra, T. A. (1976b). Field-aligned currents in the dayside cusp observed by Triad. *J. Geophys.Res.: Space Phys.*, *81*(34), 5971–5979. https://doi.org/10.1029/ja081i034p05971

Jiang, Y., Finlay, C. C., Olsen, N., Tøffner-Clausen, L., Yan, Q., and Zhang, K. (2024). Macau Scientific Satellite-1 initial magnetic field model. *Geophys. Res. Lett.*, *51*(22), e2024GL112305. https://doi.org/10.1029/2024GL112305

Kivelson, M. G., and Russell, C. T. (1995). *Introduction to Space Physics*. Cambridge, UK: Cambridge University Press. https://doi.org/10.1017/9781139878296

Langel, R. A. (1979). Near-Earth satellite magnetic field measurements: A prelude to Magsat. *Eos, Trans. AGU, 60*(38), 667–668. https://doi.org/10.1029/EO060i038p00667

Langel, R. A., Estes, R. H., Mead, G. D., Fabiano, E. B., and Lancaster, E. R. (1980). Initial geomagnetic field model from Magsat vector data. *Geophys. Res. Lett.*, *7*(10), 793–796. https://doi.org/10.1029/GL007i010p00793

Lühr, H., Southwood, D. J., Klöcker, N., Acuña, M., Häusler, B., Dunlop, M. W., Mier-Jedrzejowicz, W. A. C., Rijnbeek, R. P., and Six, M. (1986a). In situ magnetic field measurements during AMPTE solar wind Li^+ releases. *J. Geophys. Res.: Space Phys.*, *91*(A2), 1261–1270. https://doi.org/10.1029/JA091iA02p01261

Lühr, H., Southwood, D. J., Klöcker, N., Dunlop, M. W., Mier-Jedrzejowicz, W. A. C., Rijnbeek, R. P., Six, M., Häusler, B., and Acuña, M. (1986b). *In situ* magnetic field observations of the AMPTE artificial comet. *Nature*, *320*(6064), 708–711. https://doi.org/10.1038/320708a0

Lühr, H., Rother, M., Maus, S., Mai, W., and Cooke, D. (2003). The diamagnetic effect of the equatorial Appleton anomaly: Its characteristics and impact on geomagnetic field modeling. *Geophys. Res. Lett.*, *30*(17), 1906. https://doi.org/10.1029/2003GL017407

Lühr, H., and Maus, S. (2006). Direct observation of the *F* region dynamo currents and the spatial structure of the EEJ by CHAMP. *Geophys. Res. Lett.*, *33*(24), L24102. https://doi.org/10.1029/2006GL028374

Lühr, H., Xiong, C., Olsen, N., and Le, G. (2017). Near-Earth magnetic field effects of large-scale magnetospheric currents. *Space Sci. Rev.*, *206*(1), 521–545. https://doi.org/10.1007/s11214-016-0267-y

Ness, N. F. (1965). The Earth's magnetic tail. *J. Geophys. Res.*, *70*(13), 2989–3005. https://doi.org/10.1029/JZ070i013p02989

Nwankwo, V. U. J., Chakrabarti, S. K., and Weigel, R. S. (2015). Effects of plasma drag on low Earth orbiting satellites due to solar forcing induced perturbations and heating. *Adv. Space Res.*, *56*(1), 47–56. https://doi.org/10.1016/j.asr.2015.03.044

Olsen, N. (1997). Ionospheric *F* region currents at middle and low latitudes estimated from Magsat data. *J. Geophys. Res.: Space Phys.*, *102*(A3), 4563–4576. https://doi.org/10.1029/96JA02949

Olsen, N., and Stolle, C. (2012). Satellite geomagnetism. *Annu. Rev. Earth Planet. Sci.*, *40*, 441–465. https://doi.org/10.1146/annurev-earth-042711-105540

Olsen, N., Lühr, H., Finlay, C. C., Sabaka, T. J., Michaelis, I., Rauberg, J., and Tøffner-Clausen, L. (2014). The CHAOS-4 geomagnetic field model. *Geophys. J. Int.*, *197*(2), 815–827. https://doi.org/10.1093/gji/ggu033

Olsen, N. (2025). Combining polar-orbiting and low-inclination satellites — Joint analysis of data from MSS-1 and Swarm. *Earth Planet. Phys.*, *9*(3), 500–510. https://doi.org/10.26464/epp2025024

Ou, J. M., Jiang, Y., and Yan, Q. (2024). Study on the local time asymmetry of the Earth's ring currents based on multiple low-Earth-orbit satellite magnetic observations. *Sci. China Technol. Sci.*, *67*(11), 3354–3364. https://doi.org/10.1007/s11431-023-2685-1

Prölss, G. W. (2004). *Physics of the Earth's Space Environment: An Introduction*. Berlin, Heidelberg: Springer. https://doi.org/10.1007/978-3-642-97123-5

Ren, Z. Y., Huang, Y. P., Yang, C., Chen, C. J., and Zhang, K. (2025). Preliminary results suggest observations from Macau Science Satellite-1 system can improve knowledge of tidal-induced magnetic fields. *Earth Planet. Phys.*, *9*(3), 586–594. https://doi.org/10.26464/epp2025002

Rother, M., Choi, S., Mai, W., Lühr, H., and Cooke, D. (2005). Status of the CHAMP ME data processing. In C. Reigber, et al. (Eds.), *Earth Observation with CHAMP: Results from Three Years in Orbit* (pp. 413–418). Berlin: Springer. https://doi.org/10.1007/3-540-26800-6_66

Shen, X. H., Zhang, X. M., Yuan, S. G., Wang, L. W., Cao, J. B., Huang, J. P., Zhu, X. H., Piergiorgio, P., and Dai, J. P. (2018). The state-of-the-art of the China Seismo-Electromagnetic Satellite mission. *Sci. China Technol. Sci.*, *61*(5), 634–642. https://doi.org/10.1007/s11431-018-9242-0

Singer, S. F., Maple, E., and Bowen, W. A. Jr. (1951). Evidence for ionosphere currents from rocket experiments near the geomagnetic equator. *J. Geophys. Res.*, *56*(2), 265–281. https://doi.org/10.1029/JZ056i002p00265

Stolle, C., Lühr, H., Rother, M., and Balasis, G. (2006). Magnetic signatures of equatorial spread *F* as observed by the CHAMP satellite. *J. Geophys. Res.: Space Phys.*, *111*(A2), A02304. https://doi.org/10.1029/2005JA011184

Stolle, C., Michaelis, I., Xiong, C., Rother, M., Usbeck, T., Yamazaki, Y., Rauberg, J., and Styp-Rekowski, K. (2021). Observing Earth's magnetic environment with the GRACE-FO mission. *Earth Planets Space*, *73*(1), 51. https://doi.org/10.1186/s40623-021-01364-w

Tsareva, O. O., Dubinin, E. M., Malova, H. V., Popov, V. Y., and Zelenyi, L. M. (2020). Atmospheric escape from the Earth during geomagnetic reversal. *Ann. Geophys.*, *63*(2), PA223. https://doi.org/10.4401/ag-8354

Wang, F. J., Lühr, H., Xiong, C., Park, J., and Zhou, Y. L. (2023). Global characteristics of improved interhemispheric field-aligned currents and of F-region meridional currents observed by the Swarm dual-spacecraft. *J. Geophys. Res.: Space Phys.*, *128*(2), e2022JA031096. https://doi.org/10.1029/2022JA031096

Wang, Y. B., Zhang, Y., Wang, Y. J., Liu, P. F., Cheng, J. X., Li, X. Z., Tang, K., Li, L. G., and Duan, X. W. (2023). Influences of various space current systems on the geomagnetic field in near-Earth space. *Earth Planet. Phys.*, *7*(1), 93–99. https://doi.org/10.26464/epp2023010

Williams, S., Gubbins, D., Livermore, P. W., and Jiang, Y. (2025). Evaluation of the lithospheric magnetic field mapped by the first year of MSS-1 data. *Earth Planet. Phys.*, *9*(3), 614–621. https://doi.org/10.26464/epp2025033

Xiong, C., Park, J., Lühr, H., Stolle, C., and Ma, S. Y. (2010). Comparing plasma bubble occurrence rates at CHAMP and GRACE altitudes during high and low solar activity. *Ann. Geophys.*, *28*(9), 1647–1658. https://doi.org/10.5194/angeo-28-1647-2010

Xiong, C., and Lühr, H. (2023). Field-aligned scale length of depleted structures associated with post-sunset equatorial plasma bubbles. *J. Space Weather Space Clim.*, *13*, 3. https://doi.org/10.1051/swsc/2023002

Xiong, C., Wang, F. J., Huang, Y. Y., Qian, B. H., Wang, S. M., Rang, X. Y., Song, S. S., Zhou, Y. L., and Yin, F. (2025). Overview of ionospheric currents inversion by using low Earth orbit satellite magnetic observations. *Rev. Geophys. Planet. Phys. (in Chinese)*, *56*(1), 45–66. https://doi.org/10.19975/j.dqyxx.2024-013

Xu, C. Y., Lühr, H., Xiong, C., Wang, F. J., and Zhou, Y. L. (2024). Coherence of compressional Pc3-4 pulsation driven by upstream waves in topside ionosphere observed by the Swarm constellation. *J. Geophys. Res.: Space Phys.*, *129*(9), e2024JA032502. https://doi.org/10.1029/2024JA032502

Xu, W. Y. (2009). *Physics of Electromagnetic Phenomena of the Earth* (in Chinese). Hefei: University of Science and Technology China Press.

Yabuzaki, T., and Ogawa, T. (1974). Rocket measurement of *Sq* ionospheric currents over Kagoshima, Japan. *J. Geophys. Res.*, *79*(13), 1999–2001. https://doi.org/10.1029/JA079i013p01999

Yamazaki, Y., and Maute, A. (2017). Sq and EEJ—A review on the daily variation of the geomagnetic field caused by ionospheric dynamo currents. *Space Sci. Rev.*, *206*(1), 299–405. https://doi.org/10.1007/s11214-016-0282-z

Yang, Y. Y., Hulot, G., Vigneron, P., Shen, X. H., Zhima, Z., Zhou, B., Magnes, W., Olsen, N., Tøffner-Clausen, L., … Zhu, X. H. (2021). The CSES global geomagnetic field model (CGGM): An IGRF-type global geomagnetic field model based on data from the China Seismo-Electromagnetic Satellite. *Earth Planets Space*, *73*(1), 45. https://doi.org/10.1186/s40623-020-01316-w

Yang, Y. Y., Wang, J., Zhima, Z. M., Shen, X. H., Zhou, B., Yuan, S. G., Miao, Y. Q., and Xu, Y. (2024). Advancements in low Earth orbit satellite magnetic field measurements and global geomagnetic field modeling. *Rev. Geophys. Planet. Phys. (in Chinese)*, *55*(6), 652–667. https://doi.org/10.19975/j.dqyxx.2023-054

Yao, H. B., Xu, J. Y., and Zhang, K. (2025). A method for simultaneously determining Earth's magnetic field and mantle conductivity models using MSS-1 and Swarm satellite magnetic data. *Phys. Earth Planet. Inter.*, *358*, 107296. https://doi.org/10.1016/j.pepi.2024.107296

Yin F. (2010). Mathematic approaches for the calibration of the CHAMP satellite magnetic field measurements. Potsdam: University of Potsdam.

Yin, F., and Lühr, H. (2011). Recalibration of the CHAMP satellite magnetic field measurements. *Meas. Sci. Technol.*, *22*(5), 055101. https://doi.org/10.1088/0957-0233/22/5/055101

Yue, Y. C., Wei, Y., Gao, J. W., He, F., Rong, Z. J., and Wang, Y. Q. (2024). Review of secular variation studies in the South Atlantic Anomaly. *Rev. Geophys. Planet. Phys. (in Chinese)*, *55*(6), 693–704. https://doi.org/10.19975/j.dqyxx.2024-009

Zhang, K. (2023). A novel geomagnetic satellite constellation: Science and applications. *Earth Planet. Phys.*, *7*(1), 4–21. https://doi.org/10.26464/epp2023019

Zhou, Y. L., and Lühr, H. (2017). Net ionospheric currents closing field-aligned currents in the auroral region: CHAMP results. *J.Geophys. Res.: Space Phys.*, *122*(4), 4436–4449. https://doi.org/10.1002/2016JA023090